

# Nanoparticle-Based Magnetoelectric BaTiO<sub>3</sub>–CoFe<sub>2</sub>O<sub>4</sub> Thin Film Heterostructures for Voltage Control of Magnetism

Derya Erdem,<sup>†</sup> Nicholas S. Bingham,<sup>\*,‡,§</sup> Florian J. Heilitag,<sup>†</sup> Nicolas Pilet,<sup>||</sup> Peter Warnicke,<sup>||</sup> Carlos A. F. Vaz,<sup>||</sup> Yanuo Shi,<sup>†</sup> Michele Buzzi,<sup>||</sup> Jennifer L. M. Rupp,<sup>†</sup> Laura J. Heyderman,<sup>‡,§</sup> and Markus Niederberger<sup>\*,†</sup>

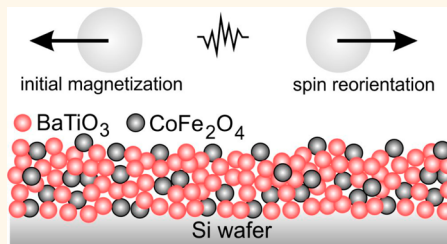
<sup>†</sup>Laboratory for Multifunctional Materials, Department of Materials, ETH Zurich, Vladimir-Prelog-Weg 5, 8093, Zurich, Switzerland

<sup>‡</sup>Laboratory for Mesoscopic Systems and <sup>||</sup>Laboratory of Electrochemical Materials, Department of Materials, ETH Zurich, Hönggerberg 64, 8093, Zurich, Switzerland

<sup>§</sup>Laboratory for Micro- and Nano-Technology and <sup>||</sup>Swiss Light Source, Paul Scherrer Institute, 5232, Villigen, Switzerland

## S Supporting Information

**ABSTRACT:** Multiferroic composite materials combining ferroelectric and ferromagnetic order at room temperature have great potential for emerging applications such as four-state memories, magnetoelectric sensors, and microwave devices. In this paper, we report an effective and facile liquid phase deposition route to create multiferroic composite thin films involving the spin-coating of nanoparticle dispersions of BaTiO<sub>3</sub>, a well-known ferroelectric, and CoFe<sub>2</sub>O<sub>4</sub>, a highly magnetostrictive material. This approach offers great flexibility in terms of accessible film configurations (co-dispersed as well as layered films), thicknesses (from 100 nm to several  $\mu\text{m}$ ) and composition (5–50 wt % CoFe<sub>2</sub>O<sub>4</sub> with respect to BaTiO<sub>3</sub>) to address various potential applications. A detailed structural characterization proves that BaTiO<sub>3</sub> and CoFe<sub>2</sub>O<sub>4</sub> remain phase-separated with clear interfaces on the nanoscale after heat treatment, while electrical and magnetic studies indicate the simultaneous presence of both ferroelectric and ferromagnetic order. Furthermore, coupling between these orders within the films is demonstrated with voltage control of the magnetism at ambient temperatures.



**KEYWORDS:** barium titanate, cobalt ferrite, multiferroic composites, nanoparticles, thin films, X-ray magnetic circular dichroism

The next-generation memory devices bring new challenges to existing materials for energy-efficient, reliable, fast, and sizable transfer of data. Promising memory applications such as magnetic random access memories (MRAM) employ ferromagnetic materials for data writing *via* switching of the magnetization states of the material. However, there are challenges related to this technology such as high energy consumption, slow writing speeds, and overheating due to high amounts of current required to generate the magnetic fields.<sup>1</sup> Ferroelectric random access memory (FeRAM) devices offer faster writing speeds *via* switching of electrical polarization states of the material.<sup>2</sup> But in this case, slower reading rates linked to destructive read operations and issues with scaling down limit the further use of this technology.<sup>3,4</sup> In this respect, multiferroic materials exhibiting both ferroelectric and ferromagnetic orders are suitable candidates for novel memory devices as compared to their semiconductor transistor-based competitors, because they offer a combination of advantages related to FeRAM and MRAM technologies enabling hybrid read–write operations.<sup>5,6</sup> Particularly interesting for miniaturization and low power con-

sumption in these devices is the voltage control of magnetism.<sup>7,8</sup> In addition, application fields for multiferroics can be potentially extended to low-voltage and fast switch speed operation of the functional oxides in other devices such as microwave reactors, sensors, transducers, actuators, and resistive switches.<sup>7,9–13</sup> Single-phase multiferroic materials are scarce due to the physics restricting the presence of both ferroelectric and ferromagnetic order,<sup>14</sup> and the few existing examples display only limited magnetoelectric coupling at low temperatures.<sup>15</sup> In comparison to single-phase multiferroics, composite materials exhibiting an indirect magnetoelectric effect offer 3–5 orders of magnitude greater coupling between electric and magnetic orders at ambient temperatures.<sup>10,16–18</sup> Such composites consist of a piezoelectric and a magnetostrictive constituent, and the coupling between different ferroic orders arises as a result of strain transfer at the phase

**Received:** August 13, 2016

**Accepted:** October 5, 2016

**Published:** October 5, 2016

boundaries of heterostructures.<sup>19,20</sup> Therefore, a high interfacial area between the two constituents is required to maximize the strain transfer. Previous work successfully demonstrated the manipulation of electric transport properties *via* controlling the degree of strain at heterostructure oxide phase boundaries for memory devices based on congruent growth of multilayers.<sup>21,22</sup> Nanocomposites composed of a mixture of the two components in various configuration schemes using nanoparticles are an attractive route to design room-temperature multiferroics.<sup>23</sup> Several studies report the preparation of composites *via* traditional solid-state reactions,<sup>24</sup> electrospinning,<sup>25</sup> vacuum-based deposition of composite thin films, and sol-gel routes.<sup>26</sup> Thin film composite structures are particularly suitable and promising for chip-device implementation.<sup>27</sup> Vacuum-based deposition methods were found to provide multiferroic thin films with large magnetoelectric coupling, enabling the realization of complex microstructures including epitaxy, texture, or columnar distribution of magnetic nanopillars in a ferroelectric matrix. However, there are issues associated with achieving the right crystallinity and stoichiometry of the phases as a result of complex growth processes, and the manufacturing costs associated with these methods are high.<sup>28–30</sup> Sol-gel routes to prepare thin films surpass the gas phase deposition methods in terms of processing costs and deposition rates. Still, processing issues associated with these techniques remain, such as the formation of side phases and the difficulty in controlling stoichiometry, film thickness, and sample crystallinity.<sup>31–35</sup> Depositing dispersions of preformed and well-defined nanoparticles to fabricate multiferroic thin films would be a way to circumvent many of these typical problems. However, nanoparticle-based liquid phase manufacture of multiferroic composites for functional applications has remained a challenge until now due to the formation of cracks, issues with surface roughness, and failure to exhibit the desired functionality.<sup>36</sup> Some of the rare, but successful examples of colloidal deposition of functional thin films from preformed nanoparticles as building blocks include  $\text{SiO}_2$ ,  $\text{TiO}_2$ ,  $\text{SnO}_2$ , and  $\text{BaTiO}_3$ , resulting in films with the desired characteristics for implementation into devices.<sup>37–41</sup>

In this paper we show that, as a result of the predefined nature of nanoparticles, crack-free multiferroic thin films in different composite geometries can be fabricated in an efficient and fast way over a wide range of thicknesses and compositions. Moreover, with the full control over phase and stoichiometry, interdiffusion or tertiary phases are avoided, which results in good contact between the piezoelectric and magnetostrictive phase. As a proof of concept, we deposited two configurations of multiferroic nanocomposite thin films on various substrates: (i) alternating stacks of piezoelectric and magnetostrictive layers and (ii) dispersion of one constituent into the matrix of the other. The ferroelectric constituent was chosen to be  $\text{BaTiO}_3$  due to its lead-free composition and attractive piezoelectric properties,<sup>42,43</sup> and  $\text{CoFe}_2\text{O}_4$  was selected as the magnetic phase because of its high magnetostriction.<sup>44</sup> We show that these thin film composites can be deposited without the formation of cracks, delamination, or occurrence of any side phases between  $\text{BaTiO}_3$  and  $\text{CoFe}_2\text{O}_4$  using a nanoparticle-based liquid phase deposition approach. Electrical and magnetic measurements as well as element-specific synchrotron studies performed on the co-dispersed nanocomposite samples provide evidence for a significant coupling between the electrical order of  $\text{BaTiO}_3$  and the magnetic order of  $\text{CoFe}_2\text{O}_4$  at ambient temperatures.

## RESULTS AND DISCUSSION

**Structural Characterization.** The  $\text{BaTiO}_3$  and  $\text{CoFe}_2\text{O}_4$  nanoparticles were synthesized using microwave-assisted non-aqueous sol-gel chemistry in acetophenone and in benzyl alcohol, respectively. The as-synthesized  $\text{BaTiO}_3$  nanoparticles have an average crystal size of approximately 13 nm, which is large enough to exhibit ferroelectric properties,<sup>35</sup> while the  $\text{CoFe}_2\text{O}_4$  nanoparticles have an average size of approximately 8 nm. Both types of nanoparticles were functionalized with 2-[2-(2-methoxyethoxy)ethoxy]acetic acid (MEEAA) and redispersed in ethanol.<sup>45</sup> For the composites involving the incorporation of  $\text{CoFe}_2\text{O}_4$  nanoparticles into a  $\text{BaTiO}_3$  matrix, co-dispersions of  $\text{BaTiO}_3$  and  $\text{CoFe}_2\text{O}_4$  were prepared by mixing the individual dispersions in the desired ratios, followed by deposition of thin films *via* spin-coating and calcination cycles. For the multilayered composites, sequential stacks of  $\text{BaTiO}_3$  and  $\text{CoFe}_2\text{O}_4$  were prepared *via* spin-coating of the individual nanoparticle dispersions with an intermediate calcination step at 500 °C. For the co-dispersed as well as for the multilayered composites, the film fabrication process was concluded by a final sintering step at 700 °C in air (see Experimental Section for details). Figure 1 displays the X-ray

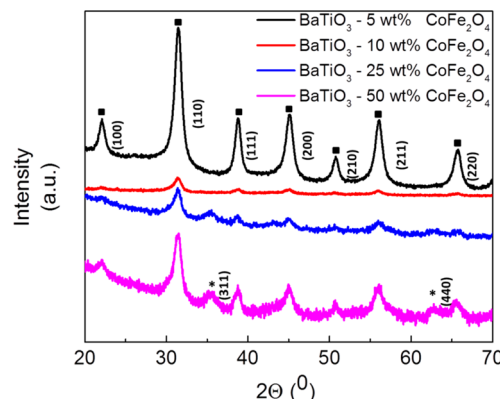


**Figure 1.** XRD patterns of  $\text{BaTiO}_3$ - $\text{CoFe}_2\text{O}_4$  co-dispersed composite thin films with thicknesses of 400–500 nm and 5–50 wt %  $\text{CoFe}_2\text{O}_4$  content. The reflections marked with a filled square denote the  $\text{BaTiO}_3$  phase, and the reflections marked with an asterisk originate from the  $\text{CoFe}_2\text{O}_4$  phase.

diffraction (XRD) patterns of the co-dispersed  $\text{BaTiO}_3$ - $\text{CoFe}_2\text{O}_4$  films of 400–500 nm thickness and with a  $\text{CoFe}_2\text{O}_4$  content of 5–50 wt %. In the samples containing 5 and 10 wt %  $\text{CoFe}_2\text{O}_4$ , only reflections from the pseudocubic  $\text{BaTiO}_3$  phase could be identified without any traces of crystalline byproducts such as  $\text{BaCO}_3$ .<sup>46</sup> The tetragonality of the  $\text{BaTiO}_3$  phase, which is essential for the presence of ferroelectric order, could not be confirmed by XRD due to the peak broadening associated with the sub-20-nm size of  $\text{BaTiO}_3$ .<sup>47</sup> In order to confirm the tetragonality, X-ray absorption spectra (XAS) at the Ti L<sub>2,3</sub> edges were acquired (see Supporting Information, Figure S1). XAS at the Ti edge for cubic crystal symmetry is known to exhibit only two absorption peaks, whereas the tetragonal symmetry displays four peaks corresponding to an additional splitting of the t<sub>2g</sub> and e<sub>g</sub> orbitals with a z-component due to off-centering of Ti<sup>4+</sup> in the tetragonal symmetry (see Supporting Information, Figure S1).<sup>48</sup> The chemical fingerprints of the  $\text{CoFe}_2\text{O}_4$  phase start to appear in the XRD patterns for the 25 and 50 wt %  $\text{CoFe}_2\text{O}_4$  samples in the form of the most intense peak of the  $\text{CoFe}_2\text{O}_4$

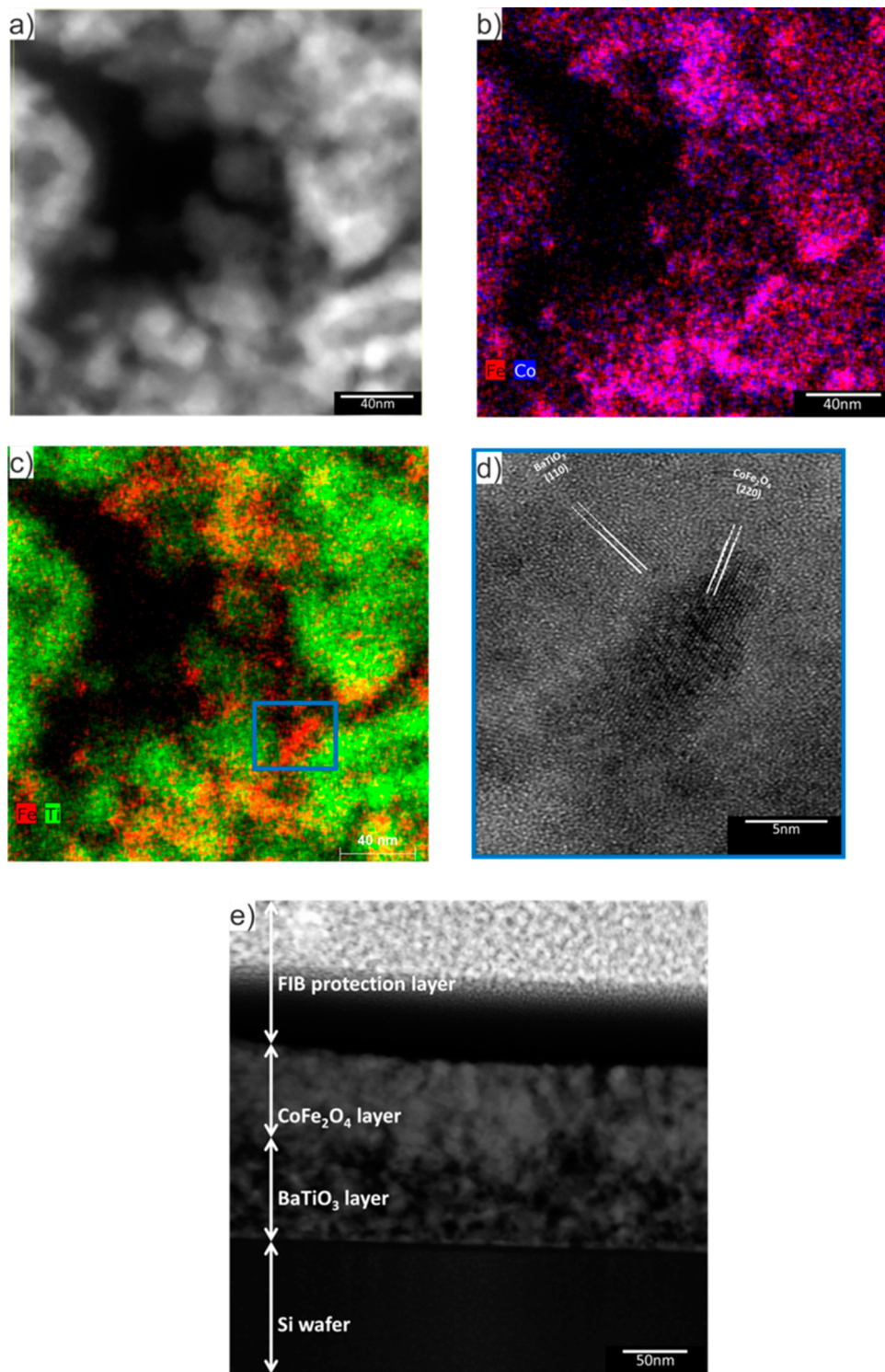


**Figure 2.** (a) STEM overview image of the EDX mapped area; (b) Fe–Co and (c) Fe–Ti elemental maps on the area shown in (a). (d) Magnified HRTEM image of the area marked with a blue box in (c), revealing the crystallographic orientations of the particles as deduced from their FFT patterns. (e) STEM image of an approximately 100 nm thick  $\text{BaTiO}_3$ – $\text{CoFe}_2\text{O}_4$  bilayer stack.

phase, namely, the (311) reflection.<sup>49</sup> The full width at half-maximum (fwhm) values of the most intense reflections for  $\text{BaTiO}_3$  are determined in order to evaluate the effect of the relative ratios of both types of particles on the crystal sizes (see Supporting Information, Table S1). The FWHM values of  $\text{BaTiO}_3$  nanocrystals increase with the  $\text{CoFe}_2\text{O}_4$  content. This indicates a refinement of the grain size when the interfacial area

between the two phases increases during sintering or due to its microstrain environment.<sup>50</sup> Considering the fact that all composites are produced starting from the same nanoparticle dispersions with the same average crystallite sizes, this observation can be explained by a restricted grain growth during sintering, cation intermixing at the  $\text{BaTiO}_3$ / $\text{CoFe}_2\text{O}_4$  interphase,<sup>30</sup> or a change in the microstrain state.<sup>51,52</sup>

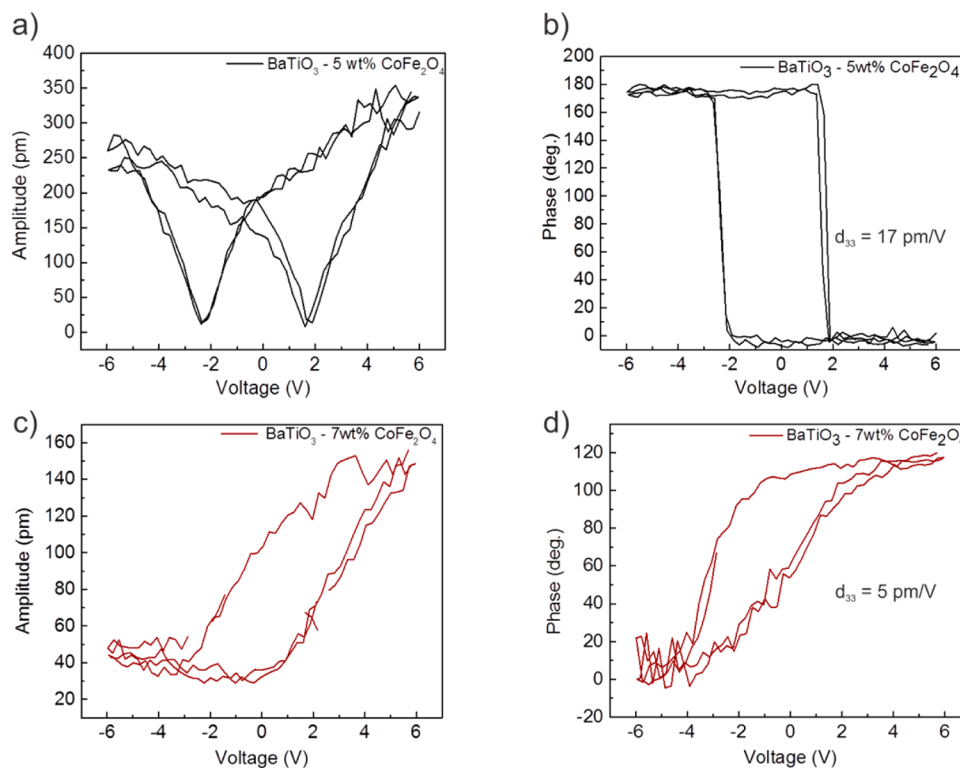


**Figure 3.** Amplitude and phase values of the piezoforce switching spectroscopy measurements on (a, b) BaTiO<sub>3</sub>-5 wt % CoFe<sub>2</sub>O<sub>4</sub> and (c, d) BaTiO<sub>3</sub>-7 wt % CoFe<sub>2</sub>O<sub>4</sub> co-dispersed thin film nanocomposite samples.

**Microstructural Characterization.** Microstructural characterization of the co-dispersed and multilayered BaTiO<sub>3</sub>-CoFe<sub>2</sub>O<sub>4</sub> composites is carried out on thin film cross sections, which are prepared by cleaving the substrate. The cross-sectional scanning electron microscopy (SEM) images of the co-dispersed composite thin films with 5–50 wt % CoFe<sub>2</sub>O<sub>4</sub> reveal crack-free, well-adhered thin films in the thickness range of 400–500 nm for all samples (see Supporting Information, Figure S2). Focused ion beam (FIB) tomography is applied to the 5 and 50 wt % co-dispersed samples to gain insight into the residual porosity in the films after sintering. The analysis of the FIB sections reveals between 30% and 50% residual porosity in the thin films (see Supporting Information, Figure S3). In a next step, the nanoparticle dispersions are used to fabricate bilayer assemblies of BaTiO<sub>3</sub>-CoFe<sub>2</sub>O<sub>4</sub> thin films in a wide thickness range from 100 nm to 1.5  $\mu\text{m}$  (see Supporting Information, Figure S4a,b and Figure 2e).

Scanning transmission electron microscopy (STEM) combined with energy dispersive X-ray (EDX) analysis is used to reveal the degree of mixing of the BaTiO<sub>3</sub> and CoFe<sub>2</sub>O<sub>4</sub> nanoparticles in the co-dispersed composites and to study the interfaces between the two types of nanoparticles after the sintering process (Figure 2a–d).

In Figure 2a, an overview STEM image, and in Figure 2b and c, the chemical maps reflecting the distributions of Ti, Fe, and Co taken in the same sample region can be seen in the co-dispersed sample with 5 wt % CoFe<sub>2</sub>O<sub>4</sub>. As expected, the elemental distribution map is dominated by Ti due to its higher content in these films. Moreover, the spatial distributions of Co and Fe overlap each other, which is expected for CoFe<sub>2</sub>O<sub>4</sub> nanoparticles. Interplanar spacings of the nanoparticles are extracted from fast Fourier transform (FFT) of the areas, where Ti–Fe elemental distribution maps overlap (marked with a blue

frame in Figure 2c), in order to correlate the composition to the crystallography at the nanoparticles' interfaces (Figure 2d). In this image, the (110) reflection of the BaTiO<sub>3</sub> phase can be identified in close proximity to (220) reflection of the CoFe<sub>2</sub>O<sub>4</sub> phase, pointing to a random mixing (*i.e.*, without any preferential orientation or epitaxy) of the two phases at the scale of individual nanoparticles. Formation of intermediate phases such as Ba(Fe<sub>10</sub>Ti<sub>2</sub>)O<sub>19</sub> has been reported to occur as a result of interdiffusion between the two phases.<sup>53,54</sup> However, in our system the sintering temperature is chosen to avoid such interdiffusion, and the HRTEM analysis confirms the absence of any intermediate phases at the BaTiO<sub>3</sub>-CoFe<sub>2</sub>O<sub>4</sub> interfaces. The absence of such an interphase is essential for an efficient strain transfer through the interface and thus to a strong coupling between the magnetic and electric degrees of freedom. In addition, HRTEM images of the co-dispersed samples with 50 wt % CoFe<sub>2</sub>O<sub>4</sub> do not reveal the evolution of any ternary phase, which means that good interfacial contacts are maintained between the piezoelectric and magnetostrictive phases (see Supporting Information, Figure S5).

High-angle annular dark field (HAADF) STEM imaging is performed on a 100 nm thick BaTiO<sub>3</sub>-CoFe<sub>2</sub>O<sub>4</sub> bilayer to characterize the interface between the two types of building blocks in the multilayered composite geometry (Figure 2e). In HAADF STEM mode, contrast occurs as a result of atomic number differences, since heavier elements scatter electrons more and therefore appear brighter. In Figure 2e, two contrasts can be distinguished, corresponding to BaTiO<sub>3</sub> and CoFe<sub>2</sub>O<sub>4</sub> layers, respectively, indicating that the layers remain phase separated after sintering.

**Optical and Electrical Characterization.** We now turn to the optical characteristics of the co-dispersed nanocomposite samples, in particular their absorption coefficients and band

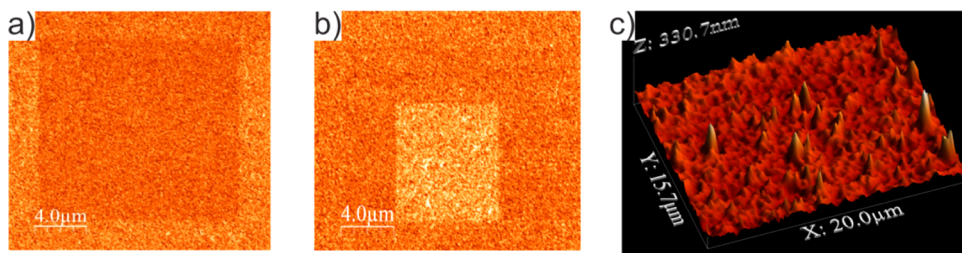


**Figure 4.** (a) Piezoresponse phase image of the sample poled using +10 V obtained at the off contact resonance of the PFM tip, where darker contrast represents the poled region. (b) Phase image of the same area, where a smaller square region (of lighter contrast in the image) was poled using -10 V in the previously poled region of a BaTiO<sub>3</sub>-5 wt % CoFe<sub>2</sub>O<sub>4</sub> sample. (c) 3D height retrace image of the sample obtained at the contact resonance of the PFM tip revealing the topography.

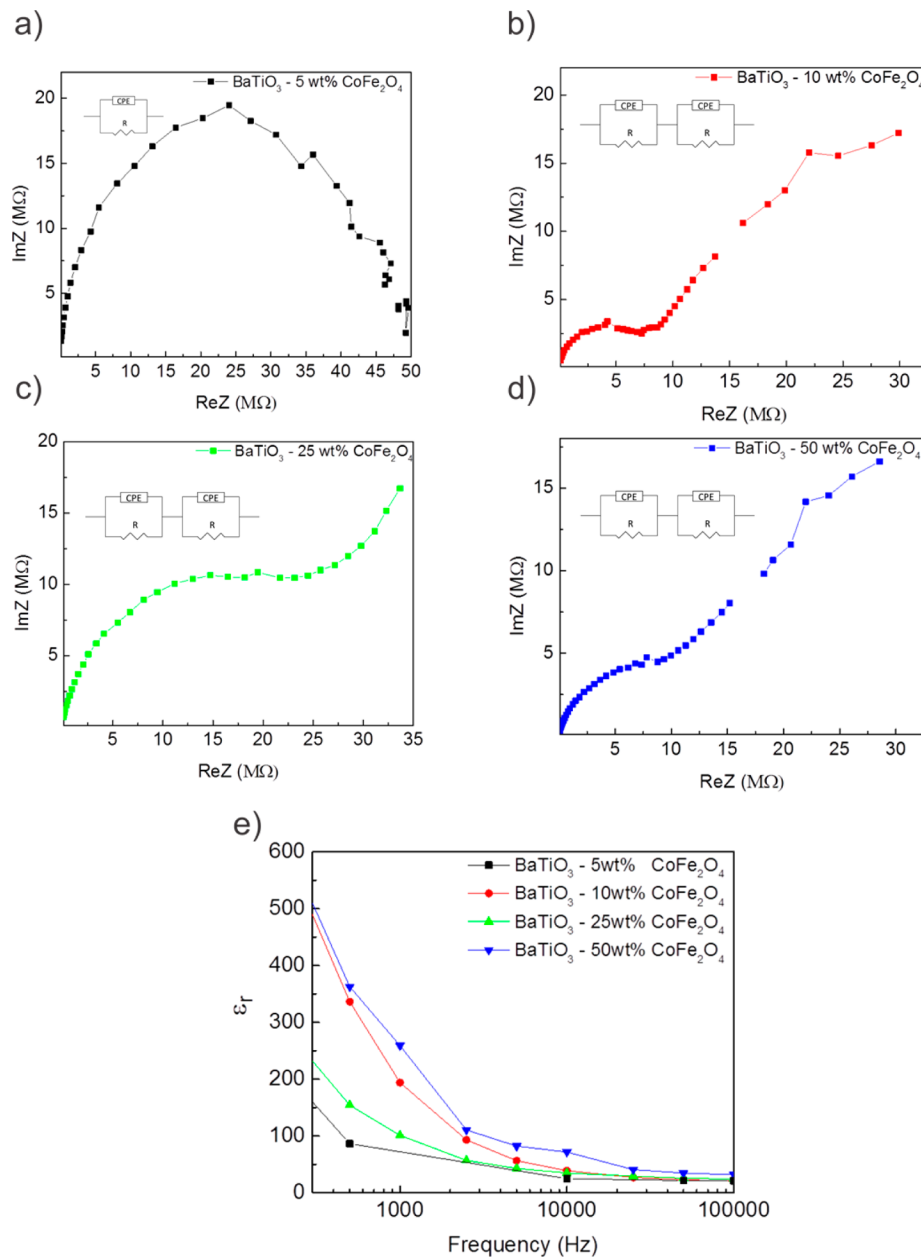


**Figure 5.** EIS measurements of the co-dispersed composite films (ca. 800 nm thick) with the composition (a) BaTiO<sub>3</sub>-5 wt % CoFe<sub>2</sub>O<sub>4</sub>, (b) BaTiO<sub>3</sub>-10 wt % CoFe<sub>2</sub>O<sub>4</sub>, (c) BaTiO<sub>3</sub>-25 wt % CoFe<sub>2</sub>O<sub>4</sub>, and (d) BaTiO<sub>3</sub>-50 wt % CoFe<sub>2</sub>O<sub>4</sub>. (e) Dielectric permittivity of the same co-dispersed thin film nanocomposites with varying CoFe<sub>2</sub>O<sub>4</sub> contents.

gaps, which are derived from the measured reflection and transmission spectra. The absorption coefficient,  $\alpha$ , is calculated

via  $\alpha d = \ln(1 - T/R)$ , where  $d$  denotes the sample thickness,  $T$  the transmission, and  $R$ , the diffuse reflection,<sup>54</sup> and is shown in

**Supporting Information**, Figure S6a. In a next step, the calculated  $\alpha$  values are inserted into Tauc plots in order to determine the band gaps (see **Supporting Information**, Figure S6b). A systematic correlation between the calculated band gaps and the amount of magnetostrictive phase was found (see **Supporting Information**, Table S2), which implies that the absorption edge of these materials can be tuned effectively by the  $\text{CoFe}_2\text{O}_4$  content, rendering these composites interesting for photocatalytic and solar-cell applications in addition to magnetoelectric devices.

The electrical characterization of the co-dispersed thin film composite samples is carried out using piezoresponse force microscopy (PFM) and electrochemical impedance spectroscopy (EIS) on the thin films of approximately 800 nm thickness. For PFM measurements, a doped diamond PFM tip is used as a top electrode, while the bottom Pt electrode was grounded. In the case of EIS measurements, circular Pt top electrodes of 0.1 mm diameter and 100 nm thickness are sputter-deposited on the samples through a shadow mask. Switching spectroscopy PFM measurements on the  $\text{BaTiO}_3$ –5 wt %  $\text{CoFe}_2\text{O}_4$  film show that the sample exhibits well-saturated hysteresis loops with ferroelectric domain nucleation voltages reaching values of 1.8 V for positive bias and 2.6 V for negative bias (**Figure 3a,b**). Similarly, the amplitude of the piezoresponse under positive bias is larger than the amplitude of the piezoresponse under negative bias. This asymmetry in the switching behavior is attributed to the asymmetry of the electrical contacts used for these measurements.<sup>55</sup> Furthermore, longitudinal shear piezoelectric coefficients are calculated from the measured amplitude and phase responses of the piezoelectric deflections. The longitudinal shear piezoelectric coefficient ( $d_{33}$ ) is a measure of the amount of longitudinal strain in the case of a vertically applied electric field. Thus, high values of  $d_{33}$  are desired for an efficient strain-mediated magnetoelectric coupling. In our case, a maximum of longitudinal piezoelectric coefficient ( $d_{33}$ ) of 17 pm/V is measured for the  $\text{BaTiO}_3$ –5 wt %  $\text{CoFe}_2\text{O}_4$  sample, which lies in the range of previously reported  $d_{33}$  values for nanocrystalline  $\text{BaTiO}_3$  in the literature.<sup>56–59</sup> As the concentration of  $\text{CoFe}_2\text{O}_4$  is increased to 7 wt %, a dramatic decrease in  $d_{33}$  is observed, which reaches a maximum value of only 5 pm/V. Additionally, the hysteresis loops become narrower and less defined (**Figure 3c** and d). This observation can be explained by the conductive character of  $\text{CoFe}_2\text{O}_4$ , which increases the leakage current in the composites, thereby preventing the buildup in electric field required for switching the  $\text{BaTiO}_3$  phase. These results suggest that the optimum  $\text{CoFe}_2\text{O}_4$  content is around 5 wt % for a sufficient dual control of electric and magnetic orders. The phase piezoresponse image taken on the electrically poled areas with  $\pm 10$  V external electrical potential proves the fully reversible and unambiguous ferroelectric nature of the sample, **Figure 4a** and b. The topography of the same region is shown in **Figure 4c**.

In the following, we turn to EIS measurements to shed more light on the electrical characteristics of co-dispersed composites with 5–50 wt %  $\text{CoFe}_2\text{O}_4$  over a wide frequency range (between 10 Hz and 1 MHz), **Figure 5a–d**. The impedance spectra of the samples with 10–50 wt %  $\text{CoFe}_2\text{O}_4$  exhibit two depressed semicircles, corresponding to different relaxation processes at the high- and low-frequency ranges. The high-frequency semicircle is assigned to the bulk properties of the composite, whereas the low-frequency semicircle appears as a result of the interfaces (grain boundaries, interphase boundaries

etc.).<sup>60</sup> The electrical circuit analogues of the impedance spectra can be fitted using two constant phase elements (CPE) with a parallel resistance connected in series, representing high- and low-frequency relaxation distributions (**Figure 5b–d**, insets). In contrast, the impedance spectrum of the 5 wt %  $\text{CoFe}_2\text{O}_4$  sample displays a single depressed semicircle with a single CPE (**Figure 5a**, inset). It can be seen that in the 10 wt % sample the percolation threshold of the  $\text{CoFe}_2\text{O}_4$  phase is exceeded and additional relaxation processes at lower frequencies associated with the grain and interphase boundaries come into play, giving rise to a second CPE in the EIS fit. A summary of the fit and error values obtained from the equivalent electrical circuits is shown in **Table 1**. Only the fitting results of the high-frequency

**Table 1. Fit Results of the High-Frequency CPE of Co-dispersed Composites**

	capacitance (pF)	n	resistance (MΩ)
$\text{BaTiO}_3$ –5 wt % $\text{CoFe}_2\text{O}_4$	3.4 (0.85%)	0.94 (0.58%)	40.1 (2.83%)
$\text{BaTiO}_3$ –10 wt % $\text{CoFe}_2\text{O}_4$	17.1 (1.7%)	0.82 (1.5%)	8.51 (3.49%)
$\text{BaTiO}_3$ –25 wt % $\text{CoFe}_2\text{O}_4$	13.6 (1.1%)	0.85 (0.87%)	25 (4.6%)
$\text{BaTiO}_3$ –50 wt % $\text{CoFe}_2\text{O}_4$	65.8 (1.01%)	0.77 (0.94%)	11.5 (2.3%)

CPE (in the 500 Hz to 100 kHz range) are shown, where the data consistency is high according to the Kramers–Kronig analysis.<sup>59</sup> The C and n values of the CPE denote the equivalent capacitance and the constant phase element exponent, respectively, which is related to the distribution of relaxation times and deviation from ideal capacitor behavior (whereby n = 1 denotes an ideal capacitor). A decrease in n can be seen upon an increase in the  $\text{CoFe}_2\text{O}_4$  content, which points to a larger deviation from ideal capacitive behavior. This phenomenon is a consequence of the inhomogeneous microstructure and related complex electrical relaxation behavior of the material above the  $\text{CoFe}_2\text{O}_4$  percolation threshold, in agreement with the previous findings in the literature.<sup>61</sup> Similarly, the resistance, R, of the CPE decreases with increasing  $\text{CoFe}_2\text{O}_4$  content, due to the lower resistance of  $\text{CoFe}_2\text{O}_4$  when compared to rather electrically insulating  $\text{BaTiO}_3$ . The leaky network formed above the  $\text{CoFe}_2\text{O}_4$  percolation threshold restricts the polarizability of the composites, in agreement with the switching spectroscopy PFM observations that  $d_{33}$  decreases with an increase in  $\text{CoFe}_2\text{O}_4$  content. The low-frequency CPEs forming above the percolation threshold have capacitance values in the 100–700 pF range, which is lower than the typically observed low-frequency capacitance values lying in the nF range (see **Supporting Information**, Table S3).<sup>60</sup> This is a common indication of residual porosity and incomplete necking in the sintered ceramics, in agreement with 30–50% porosity found in the FIB tomography images (see **Supporting Information**, Figure S3).<sup>60</sup> The dielectric permittivity is derived using the parallel plate capacitor relationship in order to investigate the frequency-dependent polarization behavior of the composites. The dielectric permittivity is characterized by a rapid decrease in the 500 Hz to 10 kHz range with increasing frequency, followed by a relatively small change for all the composite samples (**Figure 5e**). At lower frequencies, a Maxwell–Wagner polarization mechanism is active and gives rise to a large dielectric permittivity as a consequence of the effective

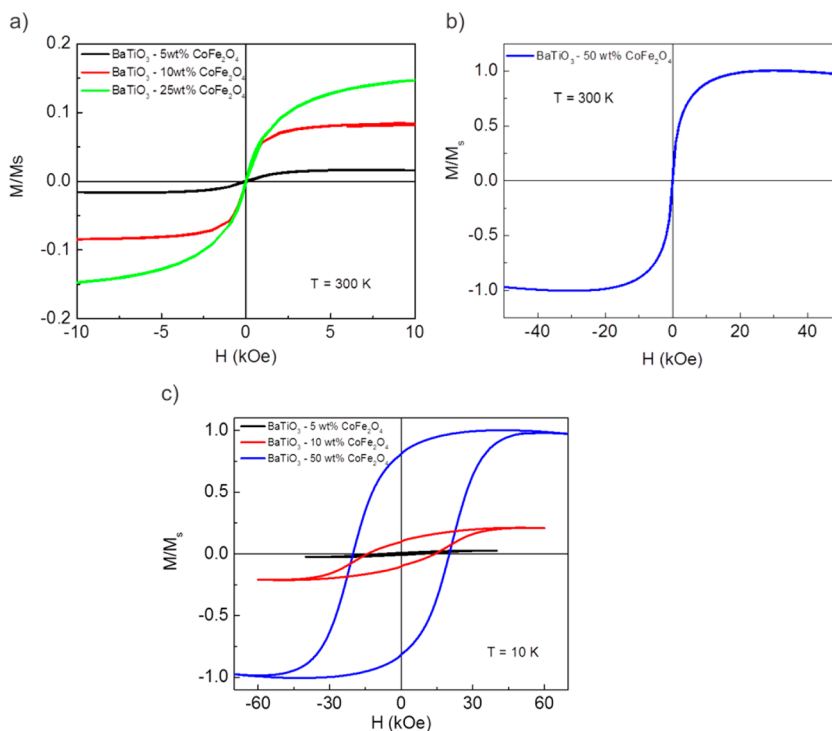


**Figure 6.** Out-of-plane hysteresis measurements on 200 nm thick co-dispersed composite films: (a)  $\text{BaTiO}_3$ -5, 10, and 25 wt %  $\text{CoFe}_2\text{O}_4$  and (b)  $\text{BaTiO}_3$ -50 wt %  $\text{CoFe}_2\text{O}_4$  measured at room temperature, (c) hysteresis measurements on  $\text{BaTiO}_3$ -5, 10, and 50 wt %  $\text{CoFe}_2\text{O}_4$  samples measured at 10 K.

interaction between the samples and the alternating electrical field, while at higher frequencies the polarization cannot follow the alternating field, resulting in a rapid decrease. At this point, it is necessary to mention that the impedance characteristics do not correlate linearly with the composition, because the dielectric permittivity depends on many factors such as grain size or porosity in addition to composition and microstructure.

**Magnetic and Magnetolectric Properties.** The room-temperature magnetic properties of the co-dispersed composites are characterized by out-of-plane hysteresis measurements on 200 nm thick films, Figure 6a–c. For these hysteresis loops, the magnetic moments of the samples are normalized with respect to the magnetic moments of the  $\text{BaTiO}_3$ -50 wt %  $\text{CoFe}_2\text{O}_4$  sample measured at saturation. The out-of-plane hysteresis loops of all samples display superparamagnetic characteristics at room temperature. A small coercivity observed in the room-temperature hysteresis curves is likely to be due to the presence of a limited number of particles that grew to sizes above the superparamagnetic size limit as a result of sintering. The coercivity of the samples in the compositional range 10–50 wt %  $\text{CoFe}_2\text{O}_4$  varies between 15 and 50 Oe, while the sample with 5 wt %  $\text{CoFe}_2\text{O}_4$  possesses a coercivity of 125 Oe (Figure 6a,b and Supporting Information, Figure S7). At lower  $\text{CoFe}_2\text{O}_4$  concentrations, the magnetic particles are more isolated, leading to a decrease in long-range magnetic dipolar interactions. However, for samples containing  $\text{CoFe}_2\text{O}_4$  above the percolation threshold (corresponding to samples with 10 wt %  $\text{CoFe}_2\text{O}_4$  and more), the  $\text{CoFe}_2\text{O}_4$  nanoparticles are in close contact with each other, and therefore they have higher dipolar interactions with an increase in the coercivity. A similar dependence of the coercivity on the magnetic ferrite content has been reported previously in the  $\text{BaTiO}_3$ - $\text{NiFe}_2\text{O}_4$  system.<sup>62</sup> As expected, the magnetization in the samples increases with increasing  $\text{CoFe}_2\text{O}_4$  content. Hysteresis measurements carried

out at 10 K show an increase in the magnetic coercivity from 8 kOe to 20 kOe with increasing  $\text{CoFe}_2\text{O}_4$  content (Figure 6c). The presence of a large coercivity indicates the freezing out of thermal excitations and the onset of stable ferromagnetic order. This is confirmed by zero field (ZFC) and field cooling (FC) curves indicating blocking temperatures in the range from 190 to 280 K (Figure 7). Such blocking temperatures correspond to magnetic particle sizes in the range of 4–8 nm, which agrees with the TEM observations.<sup>63</sup>

Element-specific magnetic characterization of the samples was performed employing X-ray magnetic circular dichroism (XMCD) measurements at room temperature at the Fe edge of the  $\text{BaTiO}_3$ - $\text{CoFe}_2\text{O}_4$  co-dispersed thin film composites with 5, 25, and 50 wt %  $\text{CoFe}_2\text{O}_4$  in an out-of-plane external

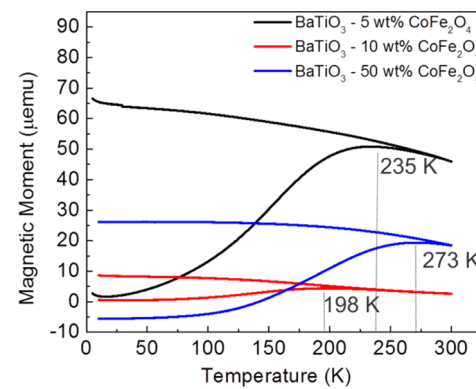


**Figure 7.** ZFC and FC curves of the  $\text{BaTiO}_3$ -5-50 wt %  $\text{CoFe}_2\text{O}_4$  co-dispersed composite thin films obtained using an external magnetic field of 1000 Oe. The thin vertical gray lines denote the maximum in the ZFC curves, corresponding to the blocking temperature.

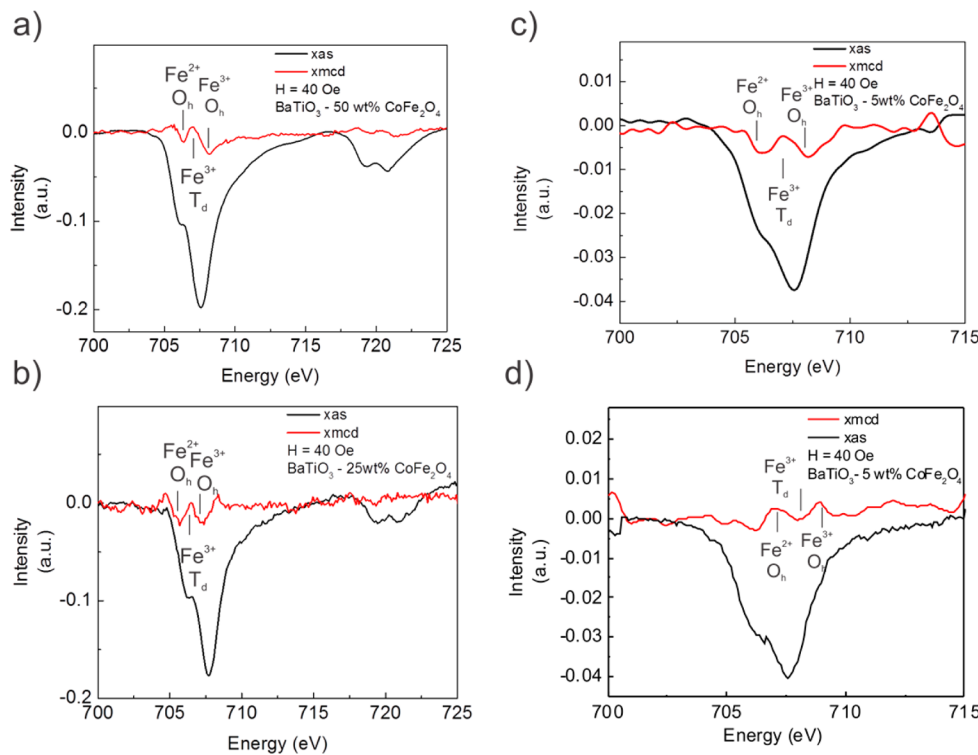


**Figure 8.** L<sub>3</sub> and L<sub>2</sub> XMCD and XAS spectra of (a) BaTiO<sub>3</sub>-50 wt % CoFe<sub>2</sub>O<sub>4</sub>, (b) BaTiO<sub>3</sub>-25 wt % CoFe<sub>2</sub>O<sub>4</sub>, and L<sub>3</sub> XMCD and XAS spectra of (c) BaTiO<sub>3</sub>-5 wt % CoFe<sub>2</sub>O<sub>4</sub> in an applied magnetic field of  $H = -40$  Oe. (d) L<sub>3</sub> edge XMCD and XAS of BaTiO<sub>3</sub>-5 wt % CoFe<sub>2</sub>O<sub>4</sub> recorded with an external magnetic field of  $H = +40$  Oe, applied in the opposite direction to demonstrate the magnetic origin of the observed XMCD signal. All samples are in the co-dispersed thin film composite configuration with an approximate thickness of 200 nm.

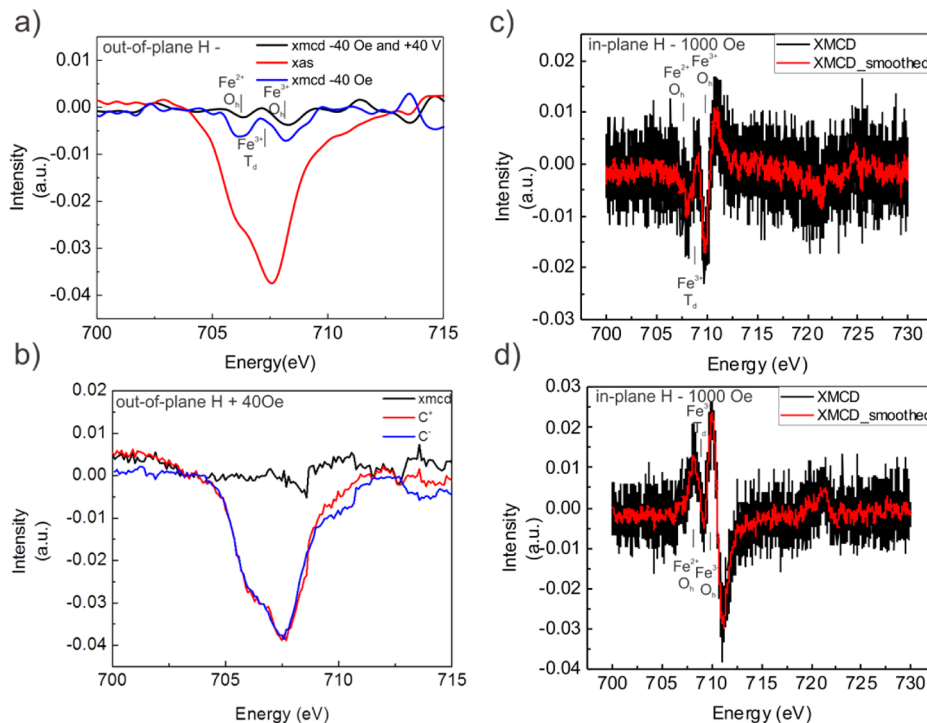


**Figure 9.** (a) L<sub>3</sub> edge XMCD spectra of BaTiO<sub>3</sub>-5 wt % CoFe<sub>2</sub>O<sub>4</sub> co-dispersed composite thin film after application of an electrical pulse of 40 V for poling (the black line). For comparison, the XMCD of the same sample obtained after applying magnetic fields only is also shown (blue line). (b) L<sub>3</sub> edge XMCD acquired under an external magnetic field of 40 Oe after application of an electrical pulse of 40 V. (c) L<sub>3</sub> and L<sub>2</sub> edge XMCD spectra of BaTiO<sub>3</sub>-5 wt % CoFe<sub>2</sub>O<sub>4</sub> co-dispersed composite thin film taken in a 1000 Oe in-plane external magnetic field. (d) The same measurement repeated after 40 V dc electrical poling, exhibiting magnetization reversal.

magnetic field of 40 Oe (Figure 8a–d). All the samples are approximately 200 nm thick. In all the XMCD spectra, three distinctive features are visible at the L<sub>3</sub> edge, assignable to Fe<sup>2+</sup> at octahedral sites and to Fe<sup>3+</sup> at tetrahedral and octahedral sites.<sup>64–66</sup> Additionally, the sign of the XMCD signal from the octahedral sites is opposite to the one from the tetrahedral sites. This reveals the ferrimagnetic nature of the cobalt ferrite, consisting of two magnetic sublattices, which are antiferromagnetically coupled to each other. The out of plane magnetization orientation given by the observed out-of-plane XMCD signal is determined by changing the direction of the external magnetic field, upon which the XMCD signal reverses (Figure 8c and d).

In a next step, the XMCD measurements are repeated following the application of an electrical field of +40 V to electrically pole the BaTiO<sub>3</sub>–5 wt % CoFe<sub>2</sub>O<sub>4</sub> sample in order to investigate the magnetoelectric coupling effect (Figure 9a–d). In-plane electric fields are applied using two top electrodes consisting of two 20 nm thick, 0.1 mm wide Cr stripes with 0.1 mm separation on the sintered thin films. Other compositions richer in CoFe<sub>2</sub>O<sub>4</sub> were not studied, because the electric poling would not be efficient due to the larger leakage behavior above the CoFe<sub>2</sub>O<sub>4</sub> percolation limit. In Figure 9a,b, the XMCD measurements carried out after applying a +40 V dc electric voltage pulse are shown for out-of-plane magnetization. The areas of the tetrahedral Fe<sup>3+</sup> peaks are normalized to the X-ray absorption peak at the L<sub>3</sub> edge in order to have a quantitative comparison of the out-of-plane XMCD signal. For magnetic fields applied in both directions before poling, the XMCD signal strength at the Fe<sup>3+</sup> site corresponds to approximately 3.4% of the total L<sub>3</sub> X-ray absorption peak. When the same XMCD measurements with a magnetic field applied in the out-of-plane direction are repeated after poling, a signal decrease takes place, up to 25% for a magnetic field applied in the negative direction, while no XMCD signal for a magnetic field applied in the positive direction can be obtained (Table 2).

**Table 2. Integral L<sub>3</sub> Edge XAS and XMCD (at Fe<sup>3+</sup> T<sub>d</sub> position) Peak Intensity Values and Peak Positions in Electronvolts (eV)**

out-of-plane magnetic field and in-plane voltage	XMCD	XAS	XMCD/XAS (%)
+40 Oe	0.00428 (707.87 eV)	0.129 (707.57)	3.3
-40 Oe	0.00503 (708.07 eV)	0.147 (707.57)	3.4
-40 Oe + 40 V	0.0032 (706.98 eV)	0.125 (707.58)	2.56
+40 Oe + 40 V	N/A	0.139 (707.48)	N/A

In order to investigate the magnetoelectric coupling in-plane, further XMCD measurements are performed employing (i) in-plane external magnetic fields of 1000 Oe and (ii) +40 V electrical poling followed by the application of a 1000 Oe in-plane magnetic field (Figure 9c and d). In this case, electric poling causes a switching in the magnetization direction of the sample when compared to the XMCD signal obtained using magnetic fields only. This finding points to the fact that in-plane electric pulses generate a 180° reorientation in the magnetization of the sample in the presence of an external magnetic field, indicating that in-plane electric poling creates an in-plane easy magnetic axis and leads to a reorientation of magnetization in this direction. This demonstrates the presence

of strong magnetoelectric coupling between the BaTiO<sub>3</sub> and CoFe<sub>2</sub>O<sub>4</sub> phases in the dilute co-dispersed thin film composite samples, enabling electric control of the magnetic order in these composites at room temperature.

## CONCLUSION

Starting from nanoparticle dispersions, we use a wet-chemical deposition method followed by sintering to fabricate BaTiO<sub>3</sub>–CoFe<sub>2</sub>O<sub>4</sub> nanocomposite thin films with different configurations including co-dispersed and multilayered composite geometries over a wide range of compositions and thicknesses for room-temperature magnetoelectric coupling. For the co-dispersed nanocomposite thin films, mixing of the two components at nanoparticle level has been demonstrated by HRTEM, providing an enlarged interfacial area for coupling. We found that there is an optimum BaTiO<sub>3</sub>–CoFe<sub>2</sub>O<sub>4</sub> ratio with a limit to the concentration of the magnetic constituent, due to increased leakage and reduced ferroelectric poling efficiency. The dilute composite with 5 wt % CoFe<sub>2</sub>O<sub>4</sub> content exhibits fully switchable ferroelectric characteristics with a *d*<sub>33</sub> maximum of 17 pm/V and a magnetic coercivity around 125 Oe, displaying ferroelectric and superparamagnetic orders at room temperature. XMCD measurements demonstrate a coupling between the electrical and magnetic degrees of freedom that manifests itself as a reorientation of easy magnetization axis from out-of-plane to in-plane upon in-plane electric poling. Hence, these BaTiO<sub>3</sub>–CoFe<sub>2</sub>O<sub>4</sub> nanocomposite thin films have the potential for making use of room-temperature electric control of magnetism, magnetic field sensors and actuators, energy harvesting, memory elements, and microwave devices.

## EXPERIMENTAL SECTION

**Materials.** Dendritic metal pieces of barium (99.99% purity), titanium(IV) isopropoxide (99.999% purity), cobalt and iron acetylacetone [Co(C<sub>5</sub>H<sub>7</sub>O<sub>2</sub>)<sub>2</sub>, >97%, Fe(C<sub>5</sub>H<sub>7</sub>O<sub>2</sub>)<sub>3</sub>, >99.8%], anhydrous benzyl alcohol (>99.8%), acetone (>99.5%), 2-propanol (>99.8%), 2-[2-(2-methoxyethoxy)ethoxy]acetic acid (technical grade), and hexane (>95% purity) were purchased from Sigma-Aldrich and used without any further purification. Ethanol (99.8% purity) was obtained from Fluka. Acetophenone (98% purity) was obtained from Acros Organics and degassed via three cycles of freeze-thaw before the synthesis. Thin films were deposited on fused silica, <100>-oriented p-type Si wafers, and Pt/TiO<sub>2</sub>/SiO<sub>2</sub>/Si wafers (MTI Corp, USA). The substrates were sonicated in acetone and 2-propanol for 5 min each prior to film deposition. For the XMCD and XAS measurements carried out in the transmission X-ray microscope, 5 × 5 mm Si frames containing 1.5 × 1.5 mm wide and 200 nm thick Si<sub>3</sub>N<sub>4</sub> membranes were used (Norcadia Inc., Canada).

**Synthesis and Dispersion of Nanoparticles.** For the synthesis of BaTiO<sub>3</sub> nanoparticles, previously published protocols are combined and adapted.<sup>67,68</sup> In a typical synthesis, 137 mg of dendritic Ba is dissolved in 5 mL of degassed acetophenone at 80 °C in an argon-filled glovebox, followed by dropwise addition of a molar equivalent of titanium isopropoxide. The mixture is transferred to a microwave vial, sealed, and exposed to microwave irradiation for 30 min at a synthesis temperature of 220 °C using a CEM Discover reactor operating at 2.45 GHz. For CoFe<sub>2</sub>O<sub>4</sub> synthesis, 353 mg of Fe(C<sub>5</sub>H<sub>7</sub>O<sub>2</sub>)<sub>3</sub> and 120 mg of Co(C<sub>5</sub>H<sub>7</sub>O<sub>2</sub>)<sub>2</sub> are mixed with 5 mL of benzyl alcohol in an argon-filled glovebox and subjected to microwave irradiation at 180 °C for 30 min in a 10 mL Teflon-capped glass vessel according to a previously published procedure.<sup>49</sup> The BaTiO<sub>3</sub> and CoFe<sub>2</sub>O<sub>4</sub> nanoparticles are centrifuged off at 4000 rpm, washed twice with ethanol, and finally sonicated for 45 min in 5 mL of 0.3 M ethanolic MEEAA solution using a Branson B3510 ultrasonic cleaner. After sonication, the nanoparticles are further stirred overnight in this mixture to ensure

sufficient binding of the stabilizing molecules to the nanoparticles' surfaces. In the next step, an excessive amount of hexane (5:1 hexane to ethanol ratio in volume) is added, and the mixture is centrifuged to separate the nanoparticles from excess stabilizing agent. Afterward, the BaTiO<sub>3</sub> and CoFe<sub>2</sub>O<sub>4</sub> nanoparticles are redispersed in ethanol with a subsequent sonication step. To obtain the thin film composite samples with different compositions, co-dispersions of BaTiO<sub>3</sub> and CoFe<sub>2</sub>O<sub>4</sub> are mixed in the desired ratios as presented in Table 3. After mixing, the co-dispersions are sonicated for 10 min and magnetically stirred for another 3–5 min.

**Table 3. Mixing Ratios of the Nanoparticle Dispersions for Co-dispersed Composites in the Range of 5–50 wt % CoFe<sub>2</sub>O<sub>4</sub>**

sample	BaTiO <sub>3</sub> (100 mg/mL)	CoFe <sub>2</sub> O <sub>4</sub> (100 mg/mL)
BaTiO <sub>3</sub> –5 wt % CoFe <sub>2</sub> O <sub>4</sub>	1 mL	0.05 mL
BaTiO <sub>3</sub> –10 wt % CoFe <sub>2</sub> O <sub>4</sub>	1.5 mL	0.15 mL
BaTiO <sub>3</sub> –25 wt % CoFe <sub>2</sub> O <sub>4</sub>	1 mL	0.33 mL
BaTiO <sub>3</sub> –50 wt % CoFe <sub>2</sub> O <sub>4</sub>	1 mL	1 mL

**Thin Film Deposition.** Both the co-dispersed and the multilayered composites are deposited using cycles of spin-coating and calcination at 500 °C on a hot plate heated to the calcination temperature at a rate of 25 °C/min. The calcination is applied after the deposition of each layer by spin-coating. The spin-coating–calcination cycles are repeated either to tune the thickness for co-dispersed composites in the range from 50 nm to 2 μm or to prepare the sequential stacks of BaTiO<sub>3</sub>–CoFe<sub>2</sub>O<sub>4</sub> multilayers. For the spin-coating, a maximum spinning speed of 1000 rpm for a total time of 20 s using a Laurell WS650 spin coater is employed. All film deposition processes prior to sintering are carried out in a laminar flow controlled synthetic air filled glovebox. Sintering in air at 700 °C for 2 h with 4 h of ramping for compaction is performed in a Nabertherm L 3/11/B170 laboratory muffle furnace to finalize the film fabrication process.

**Characterization.** XRD patterns are obtained using thin film optics (Goebels mirror on the incident side and parallel plate collimator on the diffracted side) at grazing incidence from a Panalytical X'Pert Pro diffractometer with a Cu Kα source. SEM images of the thin films deposited on Si wafers are captured at an operation voltage of 3–5 kV using a LEO 1530 scanning electron microscope. TEM images are obtained using an FEI Talos F200X microscope in the high-angle annular scanning transmission electron microscopy mode. UV-vis spectra are recorded with a JASCO V-770 spectrophotometer with an integrating spheres accessory (ILN-72S) with background and substrate correction. AFM topography images are acquired by an intermittent contact mode AFM from Asylum Cypher using AC160TS-R3 tips. The ferroelectric properties are investigated using the DART-SSPFM mode of Asylum Cypher using doped diamond PFM tips from ND-MDT on films deposited on Pt/TiO<sub>2</sub>/SiO<sub>2</sub>/Si substrates with the Pt bottom electrode grounded during the measurements. Calibration of the deflection in volts and thermal calibration of the tips are performed prior to PFM measurements, and the presented hysteresis curves are obtained in the remnant mode to minimize electromechanical tip–sample interactions with ac reading voltage between 0.5 and 1.5 V. Electrochemical impedance spectroscopy measurements are carried out using an electrochemical analyzer setup (Gamry Instruments, Reference 600) in the 10 Hz to 1 MHz frequency range with 50 mV of applied ac potential in a cross-plane measurement geometry via top and bottom electrodes on films deposited on Pt/TiO<sub>2</sub>/SiO<sub>2</sub>/Si wafers with Pt as the bottom electrode. As a top electrode, 200 nm thick circular Pt dots of 0.1 mm diameter are sputtered on the films through a shadow mask. Magnetic properties are measured using a superconducting quantum interference device (SQUID) MPMS magnetometer from Quantum Design, and ZFC and FC curves are measured in an external field of 1000 Oe. XAS and XMCD spectra of the samples are recorded using a photoemission electron microscope (PEEM) and

XMCD chamber at the SIM-X11MA beamline, and a scanning transmission X-ray microscope at the NanoXAS beamline, Swiss Light Source, Villigen, Switzerland. The spectra are taken with opposite X-ray photon helicities with a 0.1 eV step size at an applied magnetic field of 40 Oe for the measurements at the NanoXAS beamline and of ca. 1000 Oe for the measurements carried out at the SIM-X11MA beamline. XMCD was calculated using  $(I_{C+} - I_{C-})$ , where  $I_{C+}$  and  $I_{C-}$  are the intensities of right and left circularly polarized X-rays. For converse magnetoelectric effect measurements, the thin films are poled using in-plane electrical fields of 40 V prior to XMCD measurements. Cr stripes 20 nm thick, 100 μm wide, and 1 mm long are sputtered through a shadow mask onto the thin films deposited on Si<sub>3</sub>N<sub>4</sub> membranes for in-plane electrical poling. The XMCD measurements at the SIM-X11MA beamline were repeated twice to ensure the reproducibility of the results.

## ASSOCIATED CONTENT

### S Supporting Information

The Supporting Information is available free of charge on the ACS Publications website at DOI: 10.1021/acsnano.6b05469.

Ti edge XAS, X-ray peak broadening table, FIB tomography, and HRTEM images of the co-dispersed thin film nanocomposites, cross-sectional SEM images on multilayered thin film composites, and low-frequency EIS data fitting tables of the co-dispersed composites above the percolation limit ([PDF](#))

## AUTHOR INFORMATION

### Corresponding Authors

\*E-mail: binghamn@gmail.com.

\*E-mail: markus.niederberger@mat.ethz.ch.

### Notes

The authors declare no competing financial interest.

## ACKNOWLEDGMENTS

The authors are grateful to the Laboratory of Nanometallurgy, Department of Materials, ETH Zurich, for providing the AFM facility. Dr. Elena Tervoort-Gorokhova is gratefully acknowledged for the porosity and FIB tomography discussions. The TEM and FIB tomography facilities of ScopeM, ETH Zurich, are acknowledged. The authors are grateful to Dr. Alla Sologubenko for the STEM images and to Dr. Anne Greet Bittermann for the FIB tomography images and analyses. Part of this work was performed at the SIM and NanoXAS beamlines of the Swiss Light Source, Paul Scherrer Institute, Switzerland. Finally, we acknowledge financial support from ETH Zurich.

## REFERENCES

- (1) Hu, J.-M.; Li, Z.; Chen, L.-Q.; Nan, C.-W. Design of a Voltage-Controlled Magnetic Random Access Memory Based on Anisotropic Magnetoresistance in a Single Magnetic Layer. *Adv. Mater.* **2012**, *24*, 2869–2873.
- (2) Roy, A.; Gupta, R.; Garg, A. Multiferroic Memories. *Adv. Condens. Matter Phys.* **2012**, *2012*, 926290.
- (3) Ishiwara, H. Ferroelectric Random Access Memories. *J. Nanosci. Nanotechnol.* **2012**, *12*, 7619–7627.
- (4) Garcia, V.; Bibes, M. Ferroelectric Tunnel Junctions for Information Storage and Processing. *Nat. Commun.* **2014**, *5*, 4289.
- (5) Lu, X.; Kim, Y.; Goetze, S.; Li, X.; Dong, S.; Werner, P.; Alexe, M.; Hesse, D. Magnetoelectric Coupling in Ordered Arrays of Multilayered Heteroepitaxial BaTiO<sub>3</sub>/CoFe<sub>2</sub>O<sub>4</sub> Nanodots. *Nano Lett.* **2011**, *11*, 3202–3206.

- (6) Ortega, N.; Kumar, A.; Scott, J. F.; Katiyar, R. S. Multifunctional Magnetoelectric Materials for Device Applications. *J. Phys.: Condens. Matter* **2015**, *27*, 504002.
- (7) Eerenstein, W.; Mathur, N. D.; Scott, J. F. Multiferroic and Magnetoelectric Materials. *Nature* **2006**, *442*, 759–765.
- (8) Wang, L.; Wang, D.; Cao, Q.; Zheng, Y.; Xuan, H.; Gao, J.; Du, Y. Electric Control of Magnetism at Room Temperature. *Sci. Rep.* **2012**, *2*, 223.
- (9) Zavaliche, F.; Zheng, H.; Mohaddes-Ardabili, L.; Yang, S. Y.; Zhan, Q.; Shafer, P.; Reilly, E.; Chopdekar, R.; Jia, Y.; Wright, P.; Schlom, D. G.; Suzuki, Y.; Ramesh, R. Electric Field-Induced Magnetization Switching in Epitaxial Columnar Nanostructures. *Nano Lett.* **2005**, *5*, 1793–1796.
- (10) Nan, C.-W.; Bichurin, M. I.; Dong, S.; Viehland, D.; Srinivasan, G. Multiferroic Magnetoelectric Composites: Historical Perspective, Status, and Future Directions. *J. Appl. Phys.* **2008**, *103*, 031101.
- (11) Manfred, F. Revival of the Magnetoelectric Effect. *J. Phys. D: Appl. Phys.* **2005**, *38*, R123–R152.
- (12) Kubicek, M.; Schmitt, F.; Messerschmitt, F.; Rupp, J. L. M. Uncovering Two Competing Switching Mechanisms for Epitaxial and Ultrathin Strontium Titanate-Based Resistive Switching Bits. *ACS Nano* **2015**, *9*, 10737–10748.
- (13) Messerschmitt, F.; Kubicek, M.; Schweiger, S.; Rupp, J. L. M. Memristor Kinetics and Diffusion Characteristics for Mixed Anionic-Electronic  $\text{SrTiO}_{3,\delta}$  Bits: The Memristor-Based Cottrell Analysis Connecting Material to Device Performance. *Adv. Funct. Mater.* **2014**, *24*, 7448–7460.
- (14) Hill, N. A. Why Are There so Few Magnetic Ferroelectrics? *J. Phys. Chem. B* **2000**, *104*, 6694–6709.
- (15) Ramesh, R.; Spaldin, N. A. Multiferroics: Progress and Prospects in Thin Films. *Nat. Mater.* **2007**, *6*, 21–29.
- (16) Vaz, C. A. F. Electric Field Control of Magnetism in Multiferroic Heterostructures. *J. Phys.: Condens. Matter* **2012**, *24*, 333201.
- (17) Vaz, C. A. F.; Hoffman, J.; Ahn, C. H.; Ramesh, R. Magnetoelectric Coupling Effects in Multiferroic Complex Oxide Composite Structures. *Adv. Mater.* **2010**, *22*, 2900–2918.
- (18) Bichurin, M. I.; Petrov, V. M. Magnetoelectric Effect in Magnetostriction-Piezoelectric Multiferroics. *Low Temp. Phys.* **2010**, *36*, 544–549.
- (19) Chopdekar, R. V.; Malik, V. K.; Fraile Rodríguez, A.; Le Guyader, L.; Takamura, Y.; Scholl, A.; Stender, D.; Schneider, C. W.; Bernhard, C.; Nolting, F.; Heyderman, L. J. Spatially Resolved Strain-Imprinted Magnetic States in an Artificial Multiferroic. *Phys. Rev. B: Condens. Matter Mater. Phys.* **2012**, *86*, 014408.
- (20) Buzzi, M.; Chopdekar, R. V.; Hockel, J. L.; Bur, A.; Wu, T.; Pilet, N.; Warnicke, P.; Carman, G. P.; Heyderman, L. J.; Nolting, F. Single Domain Spin Manipulation by Electric Fields in Strain Coupled Artificial Multiferroic Nanostructures. *Phys. Rev. Lett.* **2013**, *111*, 027204.
- (21) Schweiger, S.; Kubicek, M.; Messerschmitt, F.; Murer, C.; Rupp, J. L. M. A Microdot Multilayer Oxide Device: Let us Tune the Strain-Ionic Transport Interaction. *ACS Nano* **2014**, *8*, 5032–5048.
- (22) Rupp, J. L. M.; Schweiger, S.; Messerschmitt, F. Strained Multilayer Resistive-Switching Memory Elements. Patent No. WO2014170023, 2014.
- (23) Etier, M.; Schmitz-Antoniak, C.; Salamon, S.; Trivedi, H.; Gao, Y.; Nazrabi, A.; Landers, J.; Gautam, D.; Winterer, M.; Schmitz, D.; Wende, H.; Shvartsman, V. V.; Lupascu, D. C. Magnetoelectric Coupling on Multiferroic Cobalt Ferrite–Barium Titanate Ceramic Composites with Different Connectivity Schemes. *Acta Mater.* **2015**, *90*, 1–9.
- (24) Shen, Y.; Sun, J.; Li, L.; Yao, Y.; Zhou, C.; Su, R.; Yang, Y. The Enhanced Magnetodielectric Interaction of  $(1-x)\text{BaTiO}_3\text{-}x\text{CoFe}_2\text{O}_4$  Multiferroic Composites. *J. Mater. Chem. C* **2014**, *2*, 2545–2551.
- (25) Xie, S. H.; Liu, Y. Y.; Li, J. Y. Synthesis, Microstructures, and Magnetoelectric Couplings of Electrospun Multiferroic Nanofibers. *Front. Phys.* **2012**, *7*, 399–407.
- (26) Liu, Y. Q.; Zhang, B.; Wu, Y. H.; Zhang, J.; Li, D.; Liu, Y.; Wei, M. B.; Yang, J. H. Synthesis, Structure, and Magnetic Studies on the  $\text{CoFe}_2\text{O}_4\text{-BiFeO}_3$  Nanocomposite Films with Different Number of  $\text{CoFe}_2\text{O}_4$  Layers. *Superlattices Microstruct.* **2013**, *61*, 174–180.
- (27) Zhao, P.; Zhao, Z.; Hunter, D.; Suchoski, R.; Gao, C.; Mathews, S.; Wuttig, M.; Takeuchi, I. Fabrication and Characterization of All-Thin-Film Magnetoelectric Sensors. *Appl. Phys. Lett.* **2009**, *94*, 243507.
- (28) Jung, C. H.; Woo, S. I.; Kim, Y. S.; No, K. S. Reproducible Resistance Switching for  $\text{BaTiO}_3$  Thin Films Fabricated by RF-Magnetron Sputtering. *Thin Solid Films* **2011**, *519*, 3291–3294.
- (29) Ferreira, P.; Hou, R. Z.; Wu, A.; Willinger, M. G.; Vilarinho, P. M.; Mosa, J.; Laberty-Robert, C.; Boissière, C.; Gross, D.; Sanchez, C. Nanoporous Piezo- and Ferroelectric Thin Films. *Langmuir* **2012**, *28*, 2944–2949.
- (30) Tileli, V.; Duchamp, M.; Axelsson, A. K.; Valant, M.; Dunin-Borkowski, R. E.; Alford, N. M. On Stoichiometry and Intermixing at the Spinel/Perovskite Interface in  $\text{CoFe}_2\text{O}_4/\text{BaTiO}_3$  Thin Films. *Nanoscale* **2015**, *7*, 218–224.
- (31) Chen, W.; Shannighrahi, S.; Chen, X. F.; Wang, Z. H.; Zhu, W.; Tan, O. K. Multiferroic Behavior and Magnetoelectric Effect in  $\text{CoFe}_2\text{O}_4/\text{Pb}(\text{Zr}_{0.53}\text{Ti}_{0.47})\text{O}_3$  Thick Films. *Solid State Commun.* **2010**, *150*, 271–274.
- (32) Andrade, H. R. C. S.; Seara, L. M.; Mohallem, N. D. S. Synthesis and Characterization of  $\text{BaTiO}_3/\text{CoFe}_2\text{O}_4$  Thin Films. *MRS Online Proc. Libr.* **2011**, *1368*, 47–52.
- (33) Xu, Y.-D.; Wu, G.; Su, H.-L.; Shi, M.; Yu, G.-Y.; Wang, L. Magnetoelectric  $\text{CoFe}_2\text{O}_4/\text{Pb}(\text{Zr}_{0.53}\text{Ti}_{0.47})\text{O}_3$  Composite Thin Films of 2–2 Type Structure Derived by a Sol–Gel Process. *J. Alloys Compd.* **2011**, *S09*, 3811–3816.
- (34) Dong, Y. L.; Du, P. Y.; Weng, W. J.; Han, G. R.; Zhao, G. L. In Situ Formation of Sol–Gel Derived  $\text{PbTiO}_3/\text{NiFe}_2\text{O}_4$  Biphase Thin Film. *J. Electrocera* **2008**, *21*, 327–330.
- (35) Erdem, D.; Shi, Y.; Heilitag, F. J.; Kandemir, A. C.; Tervoort, E.; Rupp, J. L. M.; Niederberger, M. Liquid-Phase Deposition of Ferroelectrically Switchable Nanoparticle-Based  $\text{BaTiO}_3$  Films of Macroscopically Controlled Thickness. *J. Mater. Chem. C* **2015**, *3*, 9833–9841.
- (36) Cook, K. T.; Tettey, K. E.; Bunch, R. M.; Lee, D.; Nolte, A. J. One-Step Index-Tunable Antireflection Coatings from Aggregated Silica Nanoparticles. *ACS Appl. Mater. Interfaces* **2012**, *4*, 6426–6431.
- (37) Colodrero, S.; Ocaña, M.; Míguez, H. Nanoparticle-Based One-Dimensional Photonic Crystals. *Langmuir* **2008**, *24*, 4430–4434.
- (38) Calvo, M. E.; Colodrero, S.; Rojas, T. C.; Anta, J. A.; Ocaña, M.; Míguez, H. Photoconducting Bragg Mirrors Based on  $\text{TiO}_2$  Nanoparticle Multilayers. *Adv. Funct. Mater.* **2008**, *18*, 2708–2715.
- (39) Luo, L.; Bozyigit, D.; Wood, V.; Niederberger, M. High-Quality Transparent Electrodes Spin-Cast from Preformed Antimony-Doped Tin Oxide Nanocrystals for Thin Film Optoelectronics. *Chem. Mater.* **2013**, *25*, 4901–4907.
- (40) Wang, J. C.; Zheng, P.; Yin, R. Q.; Zheng, L. M.; Du, J.; Zheng, L.; Deng, J. X.; Song, K. X.; Qin, H. B. Different Piezoelectric Grain Size Effects in  $\text{BaTiO}_3$  Ceramics. *Ceram. Int.* **2015**, *41*, 14165–14171.
- (41) Erdem, D.; Bingham, N. S.; Heilitag, F. J.; Pilet, N.; Warnicke, P.; Heyderman, L. J.; Niederberger, M.  $\text{CoFe}_2\text{O}_4$  and  $\text{CoFe}_2\text{O}_4\text{-SiO}_2$  Nanoparticle Thin Films with Perpendicular Magnetic Anisotropy for Magnetic and Magneto-Optical Applications. *Adv. Funct. Mater.* **2016**, *26*, 1954–1963.
- (42) Wang, F.; Mai, Y. W.; Wang, D.; Ding, R.; Shi, W. High Quality Barium Titanate Nanofibers for Flexible Piezoelectric Device Applications. *Sens. Actuators, A* **2015**, *233*, 195–201.
- (43) Wang, J. C.; Zheng, P.; Yin, R. Q.; Zheng, L. M.; Du, J.; Zheng, L.; Deng, J. X.; Song, K. X.; Qin, H. B. Different Piezoelectric Grain Size Effects in  $\text{BaTiO}_3$  Ceramics. *Ceram. Int.* **2015**, *41*, 14165–14171.
- (44) Mohaideen, K. K.; Joy, P. A. Studies on the Effect of Sintering Conditions on the Magnetostriction Characteristics of Cobalt Ferrite Derived from Nanocrystalline Powders. *J. Eur. Ceram. Soc.* **2014**, *34*, 677–686.
- (45) Cheema, T. A.; Garnweiter, G. Phase-Controlled Synthesis of  $\text{ZrO}_2$  Nanoparticles for Highly Transparent Dielectric Thin Films. *CrystEngComm* **2014**, *16*, 3366–3375.

- (46) Bele, A.; Cazacu, M.; Stiubianu, G.; Vlad, S. Silicone-Barium Titanate Composites with Increased Electromechanical Sensitivity. The Effects of the Filler Morphology. *RSC Adv.* **2014**, *4*, 58522–58529.
- (47) Yashima, M.; Hoshina, T.; Ishimura, D.; Kobayashi, S.; Nakamura, W.; Tsurumi, T.; Wada, S. Size Effect on the Crystal Structure of Barium Titanate Nanoparticles. *J. Appl. Phys.* **2005**, *98*, 014313.
- (48) Schmitz-Antoniak, C.; Schmitz, D.; Borisov, P.; de Groot, F. M. F.; Stienen, S.; Warland, A.; Krumme, B.; Feyerherm, R.; Dudzik, E.; Kleemann, W.; Wende, H. Electric In-Plane Polarization in Multiferroic  $\text{CoFe}_2\text{O}_4/\text{BaTiO}_3$  Nanocomposite Tuned by Magnetic Fields. *Nat. Commun.* **2013**, *4*, 2051.
- (49) Bilecka, I.; Kubli, M.; Amstad, E.; Niederberger, M. Simultaneous Formation of Ferrite Nanocrystals and Deposition of Thin Films via a Microwave-Assisted Nonaqueous Sol-Gel Process. *J. Sol-Gel Sci. Technol.* **2011**, *57*, 313–322.
- (50) Zolotoyabko, E.; Rupp, J. L. M.; Gauckler, L. J. Interrelationship Between Grain Size-Induced and Strain-Induced Broadening of X-ray Diffraction Profiles: What We Can Learn About Nanostructured Materials? *Scr. Mater.* **2012**, *66*, 190–193.
- (51) Rupp, J. L. M.; Infortuna, A.; Gauckler, L. J. Microstrain and Self-Limited Grain Growth in Nanocrystalline Ceria Ceramics. *Acta Mater.* **2006**, *54*, 1721–1730.
- (52) Rupp, J. L. M.; Fabbri, E.; Marrocchelli, D.; Han, J.-W.; Chen, D.; Traversa, E.; Tuller, H. L.; Yildiz, B. Scalable Oxygen-Ion Transport Kinetics in Metal-Oxide Films: Impact of Thermally Induced Lattice Compaction in Acceptor Doped Ceria Films. *Adv. Funct. Mater.* **2014**, *24*, 1562–1574.
- (53) Aguesse, F.; Axelsson, A.-K.; Valant, M.; Alford, N. M. Enhanced Magnetic Performance of  $\text{CoFe}_2\text{O}_4/\text{BaTiO}_3$  Multilayer Nanostructures with a  $\text{SrTiO}_3$  Ultra-Thin Barrier Layer. *Scr. Mater.* **2012**, *67*, 249–252.
- (54) Rai, R. C.; Wilser, S.; Gumiñaki, M.; Cai, B.; Nakarmi, M. L. Optical and Electronic Properties of  $\text{NiFe}_2\text{O}_4$  and  $\text{CoFe}_2\text{O}_4$  Thin Films. *Appl. Phys. A: Mater. Sci. Process.* **2012**, *106*, 207–211.
- (55) Gruverman, A.; Khoklin, A.; Kingon, A.; Tokumoto, H. Asymmetric Nanoscale Switching in Ferroelectric Thin Films by Scanning Force Microscopy. *Appl. Phys. Lett.* **2001**, *78*, 2751–2753.
- (56) Lu, H. L.; Song, S. Q.; Gu, X. F.; He, S. L.; Chen, C. L.; Song, G. B.; Cai, Z. H.; Guo, H. M.; Gao, H. J.; Sun, L. Piezoresponse Force Microscopy Study of Ferroelectric  $\text{BaTiO}_3$  Thin Film Directly Deposited on Si(001) by Magnetron Sputtering. *J. Nano Res.* **2013**, *22*, 23–30.
- (57) Mimura, K.-i.; Hiramatsu, K.; Sakamoto, W.; Yogo, T. Ferroelectric Properties of Alkoxy-Derived Transparent  $\text{BaTiO}_3$  Nanoparticle/Polymer Hybrid. *Mater. Lett.* **2012**, *89*, 40–42.
- (58) Caruntu, G.; Yourdkhani, A.; Vopsaroiu, M.; Srinivasan, G. Probing the Local Strain-Mediated Magnetoelectric Coupling in Multiferroic Nanocomposites by Magnetic Field-Assisted Piezoresponse Force Microscopy. *Nanoscale* **2012**, *4*, 3218–3227.
- (59) Boukamp, B. A. Electrochemical Impedance Spectroscopy in Solid State Ionics: Recent Advances. *Solid State Ionics* **2004**, *169*, 65–73.
- (60) Irvine, J. T. S.; Sinclair, D. C.; West, A. R. Electroceramics: Characterization by Impedance Spectroscopy. *Adv. Mater.* **1990**, *2*, 132–138.
- (61) Roy, S.; Majumder, S. B. Percolative Dielectric Behavior of Wet Chemical Synthesized Lead Lanthanum Titanate–Cobalt Iron Oxide Composite Thin Films. *Phys. Lett. A* **2011**, *375*, 1538–1542.
- (62) Grigalaitis, R.; Vijatović Petrović, M. M.; Bobić, J. D.; Dzunuzovic, A.; Sobiestianskas, R.; Brilingas, A.; Stojanović, B. D.; Banys, J. Dielectric and Magnetic Properties of  $\text{BaTiO}_3\text{-NiFe}_2\text{O}_4$  Multiferroic Composites. *Ceram. Int.* **2014**, *40*, 6165–6170.
- (63) Mohapatra, J.; Mitra, A.; Bahadur, D.; Aslam, M. Superspin Glass Behavior of Self-Interacting  $\text{CoFe}_2\text{O}_4$  Nanoparticles. *J. Alloys Compd.* **2015**, *628*, 416–423.
- (64) Moyer, J. A.; Vaz, C. A. F.; Arena, D. A.; Kumah, D.; Negusse, E.; Henrich, V. E. Magnetic Structure of Fe-Doped  $\text{CoFe}_2\text{O}_4$  Probed by X-Ray Magnetic Spectroscopies. *Phys. Rev. B: Condens. Matter Mater. Phys.* **2011**, *84*, 054447.
- (65) Moyer, J. A.; Vaz, C. A. F.; Negusse, E.; Arena, D. A.; Henrich, V. E. Controlling the Electronic Structure of  $\text{Co}_{1-x}\text{Fe}_{2+x}\text{O}_4$  Thin Films Through Iron Doping. *Phys. Rev. B: Condens. Matter Mater. Phys.* **2011**, *83*, 035121.
- (66) Moyer, J. A.; Vaz, C. A. F.; Kumah, D. P.; Arena, D. A.; Henrich, V. E. Enhanced Magnetic Moment in Ultrathin Fe-Doped  $\text{CoFe}_2\text{O}_4$  Films. *Phys. Rev. B: Condens. Matter Mater. Phys.* **2012**, *86*, 174404.
- (67) Niederberger, M.; Garnwein, G. Nonaqueous Synthesis of Barium Titanate Nanocrystals in Acetophenone as Oxygen Supplying Agent. *Mater. Res. Soc. Symp. Proc.* **2005**, *879E*, Z9.8.1–Z9.8.5.
- (68) Bilecka, I.; Djerdj, I.; Niederberger, M. One-Minute Synthesis of Crystalline Binary and Ternary Metal Oxide Nanoparticles. *Chem. Commun.* **2008**, 886–888.